Direct observational evidence of an oceanic dual kinetic energy cascade and its seasonality

Dhruv Balwada[1‡], Jin-Han Xie[2‡*], Raffaele Marino[3], and Fabio Feraco[3]

[1]Lamont-Doherty Earth Observatory, Columbia University, New York, NY, USA.
[2]Department of Mechanics and Engineering Science at College of Engineering and LTCS, Peking University, Beijing, PR China.
[3] Univ Lyon, CNRS, École Centrale de Lyon, INSA Lyon, Univ Claude Bernard Lyon 1, Laboratoire de Mécanique des Fluides et d'Acoustique, UMR5509, F-69134 Écully, France.
[‡] These authors contributed equally to this work.
[*]Corresponding author. Email: jinhanxie@pku.edu.cn.

The Ocean's turbulent energy cycle has a paradox; large-scale eddies under the control of Earth's rotation primarily transfer kinetic energy (KE) to larger scales via an inverse cascade, while a transfer to smaller scales is needed to accomplish dissipation. It has been argued, using numerical simulations, that fronts, waves and other turbulent structures can produce a forward cascade of KE toward dissipation scales. However, this forward cascade and its coexistence with known inverse cascade were not confirmed in observations. Here we present the first evidence of a dual KE cascade in the Ocean by analyzing velocity measurements from surface drifters released in the Gulf of Mexico. Our results show that KE is injected at two dominant scales and transferred to both large and small scales, with the downscale flux dominating at scales smaller than 1-10km. The cascade rates are modulated seasonally, with stronger KE injection and forward transfer during winter.

The oceanic circulation is primarily forced at scales of $O(1000)$ km by the winds, tides, and solar heating, and dissipated by friction at scales of $O(1)$ mm. Ocean turbulence helps to redistribute the energy across scales, populating the range between forcing and dissipation scales, and also promoting the exchanges between potential and kinetic energy reservoirs (*1*). The bulk of the oceanic kinetic energy resides in flows with horizontal scales of hundreds of kilometers (*2*), the so-called mesoscales. These flows are characterized by rapid rotation and strong stratification, so their dynamics are well described by the quasi-geostrophic (QG) theory. These dynamics dictate a general tendency of the oceanic flow to transfer kinetic energy from small to large scales through the inverse cascade (*3, 4*), and suggest a rather steep drop-off in kinetic energy at the smaller scales, following a k^{-3} spectrum. Consequently, according to QG dynamics, the mesoscale kinetic energy is expected to be dissipated primarily by boundary friction. However, estimates suggest that dissipation through boundary friction accounts for only one-tenth of the total energy injection, raising a puzzle about the dissipation mechanisms (*5*). To resolve this puzzle, there must be mechanisms not described in the QG theory for transferring kinetic energy from large to small scales, through a forward cascade.

Observations and high-resolution simulations have shown that the range of scales referred to as the submesoscales, scales between 3D turbulence (O(50-100)m) and the mesoscale (O (100m)), are quite energetic in the surface ocean (*6, 7*), often following a k^{-2} spectral slope for horizontal kinetic energy and buoyancy variance, and show a pronounced seasonal modulation in energy levels (*8–11*). These scales are thought to be energized through mesoscale driven straining of buoyancy fronts (*12, 13*) or mixed-layer instabilities (*14, 15*), which acts to release the available potential energy stored in mixed layers. The latter mechanism is now routinely implicated for the observed seasonality at these scales. The shallow spectral slope implies that the Rossby number, a ratio of inertial force to the Coriollis force, can become O(1) at these scales, which suggests that the submesoscale flows can escape the constraints of geostrophic

2

balance and potentially transfer kinetic energy to smaller scales (*16, 17*). These flows are also expected to play an important role in the mixed layer restratification (*18*), and transporting tracers between the mixed layer and the interior (*19, 20*).

The suggestion that submesoscale flows at the surface can result in a forward cascade of kinetic energy has been confirmed in high-resolution ocean model runs, e.g. (*21, 22*). These simulations show that the surface kinetic energy flux can undergo a dual cascade, flowing up-scale at large scales and downscale at small scales, with the forward cascade being present at scales roughly smaller than O(10)km. The kinetic energy reservoir is supplied by conversion from available potential energy to kinetic energy, and the ageostrophic flow is crucial for the forward cascade to emerge. In this phenomenology the surface kinetic energy does not develop an inertial range, as it is not a conservative quantity because of exchanges with the underlying interior (*16*). Additionally, direct numerical simulations of rotating stratified turbulent flows in the appropriate parameter regimes (*23, 24*) have indicated that a dual energy cascade can also be sustained in the ocean interior. While evidence and mechanistic understanding of the dual cascade in the ocean has been made possible by sophisticated high-resolution simulations, there are no observational studies that have been able to unambiguously confirm its presence yet.

Estimating the inter-scale energy transfers in the ocean from observations is extremely challenging, due to the fact that conventional spectral flux estimation methods used to analyze numerical simulations (*25*) require the availability of synoptic measurements on a regularly sampled grid and over a fairly large region; technology to collect such measurements at sub-mesoscales is not available at this time (*17*). Sea surface height (SSH) measurements from satellites come the closest to producing datasets that are amenable to spectral flux calculations, they provide gridded estimates of surface geostrophic velocity with a nominal spatial resolution of O(100)km and time resolution of a week. Spectral flux calculations from SSH-based velocities have provided clear evidence for the presence of an inverse energy cascade at scales larger

3

than 100km, and suggested the presence of a forward energy and enstrophy cascade at scales smaller than 100km (*26, 27*). However, the conclusions about scales smaller than 100km are debatable because these estimates rely on the assumption of geostrophy to estimate the velocity from SSH and due to strong sensitivity to the gridding and interpolation methods (*28*). In coastal locations, high-frequency radars have been used to estimate the surface velocity fields with resolutions of a few kilometers and can be used for estimating the spectral flux, but are limited in coverage to within $\sim 10 - 100$km off the coast (*29*). Velocity estimates from a mooring array were used in a recent study to suggest the presence of a forward cascade at the submesoscales in the spring (*30*) using a frequency decomposition. However, this work relied on assuming a connection between the temporal and spatial scales due, and did not directly probe the spatial structure of how kinetic energy is transferred.

An approach to probing the properties of the inter-scale energy transfers using observations has been to use third-order structure functions (*31, 32*), which can be estimated from un-gridded or scattered measurements under the assumption of statistical homogeneity. Surface drifters, released in large clusters, have allowed for a characterization of the energy cascades by estimating third-order velocity structure functions (SF3, see Methods) (*32–34*). These studies, all from drifter releases in the Northern Gulf of Mexico, have suggested that a forward cascade exists at scales smaller than O(1-10)km based on a sign reversal in SF3 around this scale, and have quantified the forward energy flux based on exact formulae for the SF3 derived using inertial-range arguments. A major improvement of this methodology for the quantification of the energy fluxes is due to Xie and Bühler 2019 (*35*), who proposed a forcing-scale resolving SF3 formulation able to capture the simultaneous bidirectional energy transfer. This formulation applies to a range beyond the inertial range, and its implementation does not require the identification of inertial ranges in order to fit SF3 expressions with power-law functions. Meanwhile, it also allows the estimation of energy injection scales, which is important for gaining a

4

better understanding of the turbulent cascades.

Here we apply these new theoretical insights to two surface drifter data sets, collected during the Grand Lagrangian Deployment (GLAD) and the Lagrangian Submesoscale Experiment (LASER) in the Gulf of Mexico in summer and winter, respectively. We focus specifically on velocity estimated from surface drifter trajectories in the northern Gulf of Mexico, in waters that are deeper than 500m and away from the continental shelf. Our results confirm the presence of a seasonal modulation of submesoscale surface kinetic energy (KE), and more importantly, for the first time, characterize and quantify the inter-scale energy transfer simulataneously to the large and small scales, at the submesoscales in the ocean. The results confirm the existence of a dual cascade of KE at the ocean surface, which is energized primarily at scales close to the mixed-layer and interior deformation radii, with the transition of energy flux direction happening around a scale where the local Rossby number is of O(1). Energy injection and the KE flux are stronger in the winter than in the summer, and the scale of energy-injection likely corresponding to the mixed layer baroclinic instability also moves to larger scales in the winter relative to the summer.

Results

GLAD and LASER experiments

We analyze data from surface drifters that were deployed in the Northern Gulf of Mexico, in a region usually to the north of the Loop Current. The surface drifters were deployed as part of the Grand Lagrangian Deployment (GLAD) in Summer/July-August 2012 (*36*) and the Lagrangian Submesoscale Experiment in Winter/January-February 2016 (*37*), which are to-date the largest simultaneous drifter deployments. Over the course of the 3-4 months that the drifters were active they dispersed to span a large part of the Gulf of Mexico, and this long-term dispersion was largely influenced by the basin-scale and mesoscale circulation in the region (Figure 1). The

5

Grand Lagrangian Deployment (GLAD)
Summer 2012

LAgrangian Submesoscale ExpeRiment (LASER)
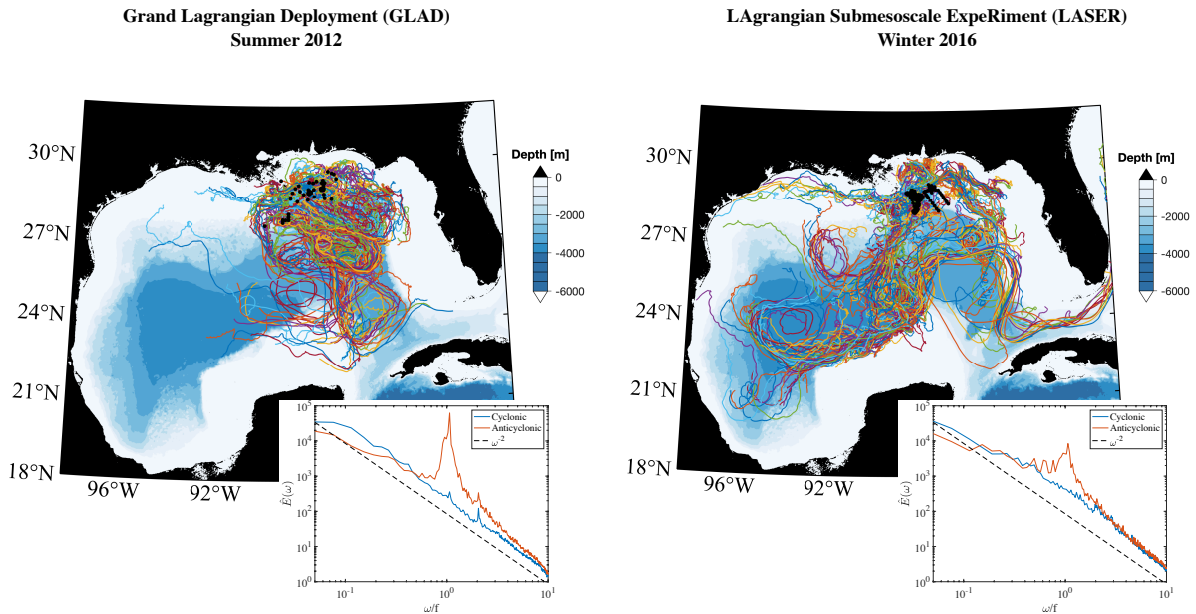**Winter 2016**

Figure 1: **Spatial distribution of the drifters.** Drifter tracks and the Lagrangian frequency spectra (inset plots) for the GLAD (a) and LASER (b) experiments. Black dots indicate the deployment locations, and the colored contours indicate the bathymetric depth. In our study we only considered the sections of the drifter tracks that were in water deeper than 500m, and in between east of 84-91°W and north of 24°N.

part of the data analyzed here comes mainly from the initial few weeks after the deployments when the drifters are relatively close to each other, and contained mostly in the Northern Gulf. We also excluded the drifter tracks when they went in waters shallower than 500m or ventured west of 91°W, east of 84°W, or south of 24°N, as we want to focus on the dynamics away from the continental shelf and in the NorthEastern GOM.

The atmospheric forcing during summer deployment was characterized by relatively weak winds ($\sim$ 5 m/s), while the winter deployment experienced stronger winds ($\sim$ 8 m/s) and severe storms. The summer months in the northern GOM are also characterized by very shallow mixed layers ($\sim$ 10m) and lateral buoyancy gradients that are produced by the inflow of fresh water from the Mississippi river delta, while in the winter the mixed layer deepens ($\sim$ 80m) and the

lateral buoyancy gradients are primarily a result of temperature variations (*34, 38*). The drifters tracked the flow in the top 0.60 m of the water column (*39*). The summer drifter trajectories and velocities show a marked presence of inertial oscillations (Figure 1 inset), and the amplitude of these oscillations are damped by about an order of magnitude in the winter; likely in response to the seasonal modulation of the mixed layer depth (*40*).

The scale-wise variation of the kinetic energy content in the surface ocean will be assessed by means of the second-order velocity structure functions, and then a novel approach based on the third-order structure functions will be implemented to get insights in to the transfer and injection of kinetic energy as a function of length scales (see method for details).

Seasonal modulation of surface kinetic energy

The second-order structure functions (SF2; $D_{LL}(r) = \langle \delta u_L^2 \rangle$, $D_{TT}(r) = \langle \delta u_T^2 \rangle$), which reflect how kinetic energy is distributed as a function of scales, show a marked change in properties between summer and winter (Figure 2)[1]. The detailed definition of SF2 can be found in the Method section (cf. (1)). The total SF2 ($D_{tot} = D_{LL} + D_{TT}$), reflective of the total horizontal kinetic energy, in winter is larger by a factor of approximately 2 at scales on the O(100m-10km), while the non-divergent or rotational part of SF2 (discussed more in the next paragraph) in winter is around 10 times larger at those scales (Figure 2b). The larger scales, O(20-100km), show a slight reduction of total SF2 in the winter; this is most likely a reflection of the synoptic modulation in the mesoscale field rather than a signal associated with the seasonal variability. The smallest scales, O(<100m), also show a slight reduction of total SF2 in winter, which is likely related to the precise deployment conditions and spatial variability since these smallest range of scales are sampled for very short periods after deployment. We also defined a scale-

---

[1]Some aspects of the second order structure functions presented here have been discussed for the individual experiments or for a shorter range of scales in previous studies, eg (*32–34, 36, 41*), but this is the first comparative synopsis between seasons using the Helmholtz decomposition.
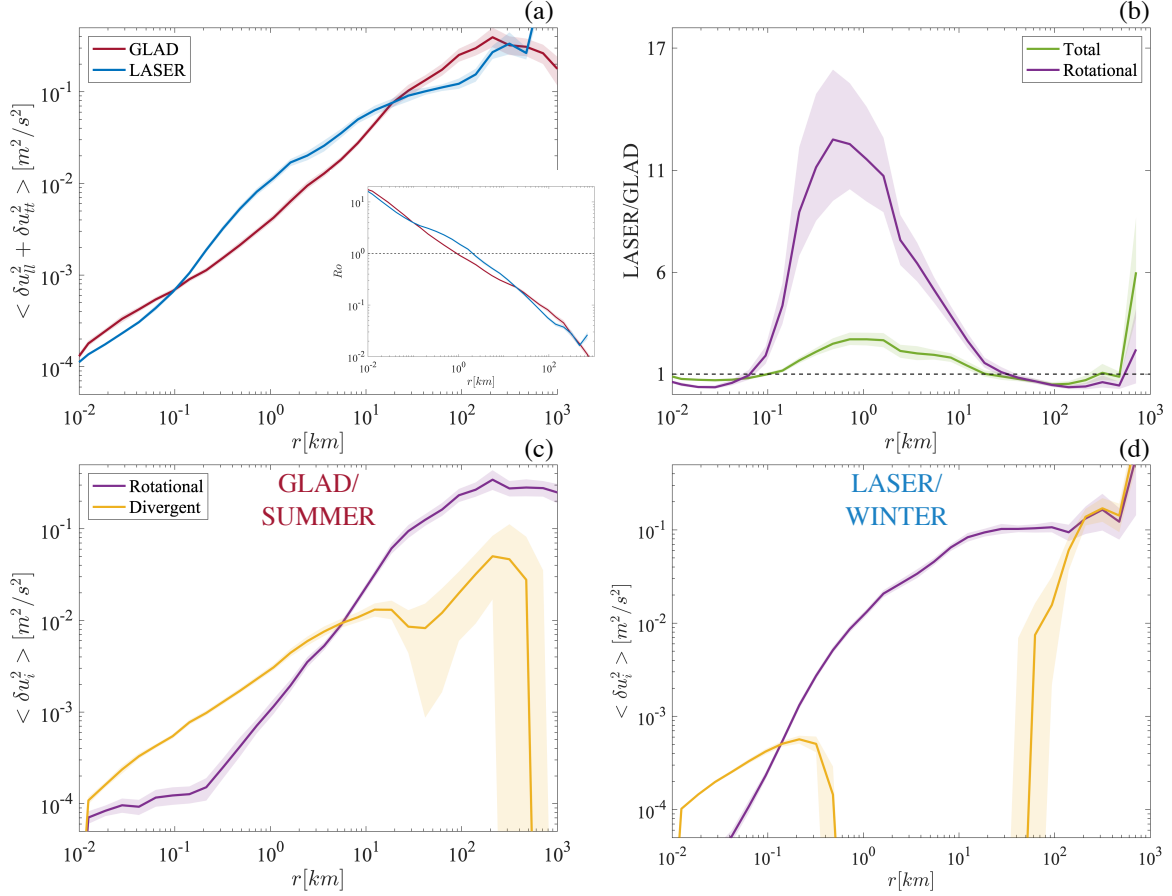
Figure 2: **Distribution of kinetic energy as a function of scale represented using second-order structure functions.** (a) The total, sum of the longitudinal and transverse, second-order structure function ($D_{tot}(r) = D_{LL}(r) + D_{TT}(r)$) as a function of separation scale for the GLAD and LASER experiments. The inset shows the Rossby number, defined as $Ro = \sqrt{D_{tot}}/fr$, as a function of scale, with the dashed horizontal line indicating $Ro = 1$. (b) The ratio of total and rotational second order structure function from the LASER and GLAD experiments, with dashed horizontal line indicating a ratio of 1. (c, d) The decomposition of the total structure function into the rotational and divergent components, Helmholtz decomposition, for the GLAD and LASER experiments.

8

dependent Rossby number using the total SF2, as $Ro = \sqrt{D_{tot}(r)}/fr$ with f being the Coriolis frequency and r being the separation scale. This Rossby number is O(1) at scales smaller than 1-5 km, and is slightly greater in the winter than the summer following the seasonal modulation of the total SF2.

To gain further insight into the type of the flows that contribute to the total SF2, we decomposed it into the rotational (D_R) and divergent (D_D) contributions using a Helmholtz decomposition (*42*). The relative contribution from the divergent and rotational parts of the flow changes significantly between seasons, and indicates a dramatic change in the flow dynamics between summer and winter (Figure 2c,d). In summer the divergent motions dominate up to scales of 5km, while in winter dominance of divergent motions is limited to scales smaller than about 100m. Non-physical peculiarities in the divergent component, such as small negative values (at scales larger than 500km in summer and scales between 500m-50km in winter) or comparable values at the largest scales (scales larger than 200km in winter) are likely a result of slight breakdown of assumptions of homogeneity and isotropy that are required for the Helmholtz decomposition (*43*); we do not expect these issues to impact the qualitative aspects of these results (*41*). The power-law behavior of the rotational SF2 also shows a marked change between seasons. While both seasons show that the rotational SF2 has a shallow slope, suggestive of an inverse energy cascade, at large scales and steeper slope at smaller scales, the scale where this slope changes shifts from approximately 1km in winter to around 20km in summer.

The second-order structure functions indicate that the submesoscale flow, roughly defined as scales smaller than 50km, is more energetic in winter than the summer, and this is primarily a result of strengthening of the rotational (non-divergent) flow. The change in power-law behavior of the rotational SF2 between seasons suggests that a higher amount of kinetic energy is injected into the non-divergent part of the flow near the mixed-layer deformation radius, O(1-10km), in the winter, and the cascade of this energy is strong enough to paint the distribution

9

of kinetic energy in the submesoscales. It is also quite striking that the energized winter flow is dominantly rotational, which suggests a dominance of balanced flows likely energized by mixed-layer instability, while the summer flow has a large contribution from divergent modes suggesting an abundance of ageostrophic motions, potentially resulting from strain-driven frontogenesis and internal waves (also highlighted in the Lagrangian frequency spectra in Figure 1).

The results from the surface drifters suggest that the seasonality of the surface flows in this part of the Gulf of Mexico are qualitatively similar to other parts of the ocean that have a large seasonal modulation of mixed-layer depth (*7, 15*).

Seasonality of inter-scale kinetic energy transfers

The third-order velocity structure functions (SF3; $V(r) = \langle \delta u_L^3 \rangle + \langle \delta u_L \delta u_T^2 \rangle$) are a metric that can be associated with the turbulent kinetic energy transfer rate (*25*), and their sign, under certain hypothesis, is associated with the direction of the kinetic energy transfer – with a negative SF3 indicating a forward or downscale transfer of energy and vice-versa. The GLAD experiment, conducted in the summer, provided the first observational evidence in the ocean that a wide range of scales, O($<$1km), had a negative SF3 (*32, 33, 44*), which is emblematic of a forward cascade of energy. The LASER experiment conducted a few years later in the winter season further solidified the generality of this observational result (*34, 45*), and also showed a seasonal modulation in the length scale where the sign change happens (Figure 3). A similar result showing negative values of SF3 at smaller scales had been observed in the atmosphere about two decades earlier (*31*).

The interpretation, in these previous studies, of the direction of kinetic energy transfer based on the sign of the SF3 is rooted in classic inertial-range theories, e.g. Kolmogrov's 4/5th law (*46*). These interpretations are potentially suspect, or are at least only qualitatively correct,
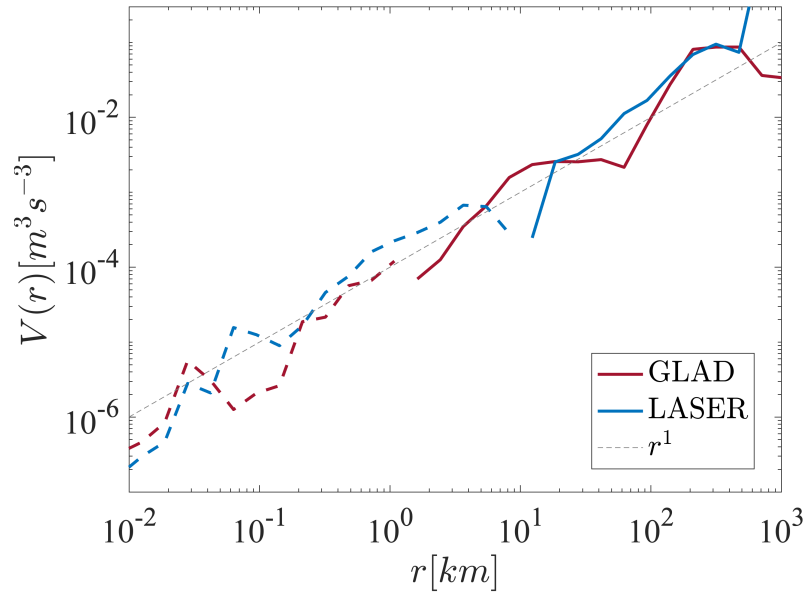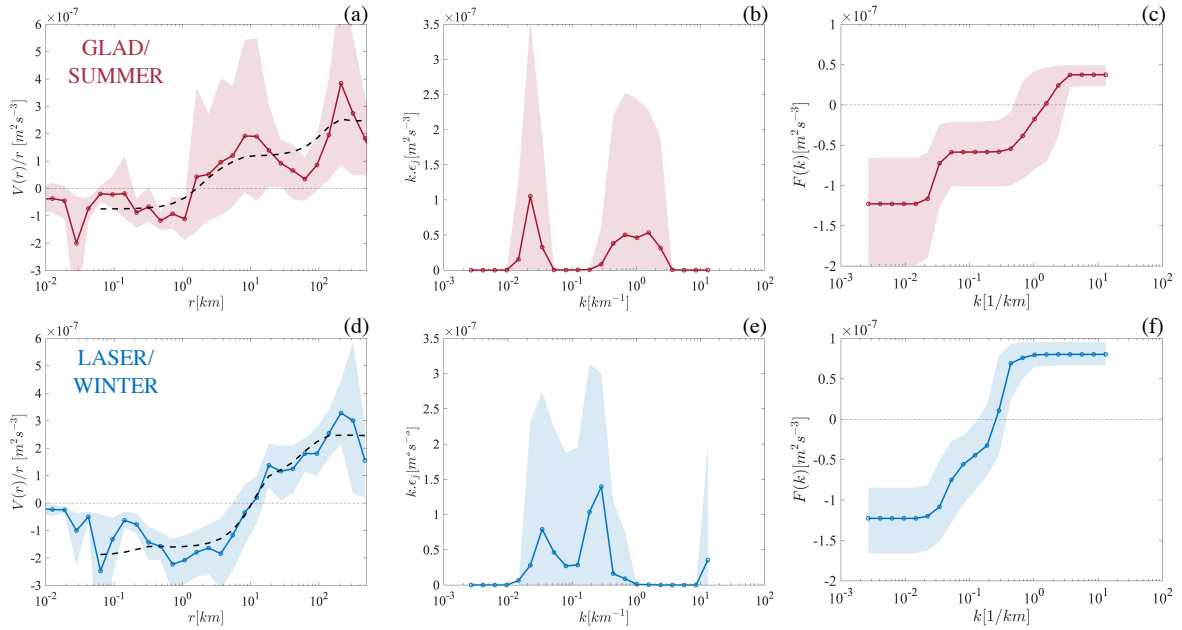
Figure 3: **Third-order structure functions** ($V(r) = \langle \delta u_L^3 \rangle + \langle \delta u_L \delta u_T^2 \rangle$) **from GLAD and LASER.** Absolute value of $V(r)$ is plotted, and the range of scales where $V(r)$ is negative are indicated as dashed lines. A linear power law is also indicated as a dashed line for reference. Error estimates are not plotted here because they can not be represented properly on the logarithmic axis near the scale where the sign changes; the error estimates on these quantities can be seen in Figure 4a,d.

Figure 4: **Estimates of spectral flux and corresponding parameters from third-order structure functions for the GLAD/Summer (top; a-c) and LASER/Winter (bottom; d-f) experiments.** (a,d) The normalized third-order structure function $(V(r)/r)$ and the fit, dashed black line, over scales of 50 m-500 km. (b,e) The estimated energy injection as a function of wavenumber, plotted in variance-preserving form to account for the logarithmic x-axis. Variance-preserving form accounts for the squeezing of the x-axis on a logarithmic scale and ensures that these panels can be visually interpreted such that the amount of energy injected corresponds to the area under the curve. (c,f) Spectral flux as a function of wavenumber. The positive and negative values denote upscale and downscale fluxes, respectively.

when inertial ranges cannot be clearly identified, or when the assumptions used to reach inertial range arguments, e.g. purely two- or three-dimensional flow or asymptotic separation from forcing scales, are not satisfied. To overcome this major limitation we use a new theoretical framework developed by Xie and Bühler 2019 (*35*) that allows us to directly infer the spectral fluxes from SF3, under the conventional assumptions of isotropy and homogeneity. In this framework, the spectral flux ($F(k)$) is defined by the corresponding energy injection rates ($\epsilon(k)$) at wavenumber k (corresponding to scale $l = 1/k$), and the upscale energy transfer rate (ϵ_u), which are the parameters that represent the shape of $F(k)$. This spectral flux was analytically transformed to the corresponding SF3 in terms of the same parameters. The observational estimate of the SF3 can then be fitted using this analytical form, and all the parameters and thus the corresponding spectral flux can be inferred. To avoid amplifying small-scale error in the inversion process we made a physically motivated and pragmatic assumption that over the range of observed scales the energy injection is positive and only adds energy to the surface flow, which is equivalent to assuming that the spectral flux is an increasing function of wavenumber and that all the dissipation and extraction of kinetic energy out of the surface flow takes place outside the range of scales where the fitting is done. This is very well justified for dissipative mechanisms, which are active at scales much smaller than the ones observed here, but any transfer from kinetic energy to potential energy over the range of fitting scales has been ignored here (further details in Methods and SI). Even with this assumption the fitted SF3 matches the observed SF3 relatively well, capturing the broad structure within errorbars, and without fitting every small detail (Figure 4a,c).

The estimated parameters provide us with two crucial physically relevant measures of the flow dynamics, the distribution of energy injection rate (Figure 4b,c) and the spectral flux as a function of spatial scale or wavenumber (Figure 4e,f). The energy injection shows two distinct peaks, one associated with smaller scales and another with larger scales. The large-scale peak is

occurs around 40-50km, spreading between 20-100km, and does not vary significantly with the season. In contrast, the smaller-scale energy injection is modulated seasonally. In summer the energy injection peaks around 1km and is spread between 500m-5km, while in winter the peak is shifted to about 5km and is spread between 1km-10km. In summer the small- and large-scale peaks are distinct, while in winter the small scale energy injection is stronger in amplitude than summer and the small and large scale energy injections show a tendency to partially overlap. The scale where the spectral flux changes from being negative (upscale transfer) to positive (downscale transfer) is also approximately the same as the scale where the small-scale energy injection peaks, which is further correlated with the scale where the Rossby number starts to become $O(1)$ (Figure 2a inset).

Experiment/ Season	Upscale energy transfer rate, ϵ_u $[m^2/s^3]$	Large scale energy injection rate (10km -100km) $[m^2/s^3]$	Small scale energy injection rate (100m - 10km) $[m^2/s^3]$
LASER/ Winter	$1.23\,(0.85-1.66)\times10^{-7}$	$0.78\,(0-1.36)\times10^{-7}$	$1.25\,(0.84-1.73)\times10^{-7}$
GLAD/ SUMMER	$1.23\,(0.66-1.99)\times10^{-7}$	$0.64\,(0-1.56)\times10^{-7}$	$0.96\,(0.53-1.41)\times10^{-7}$

Table 1: Estimated upscale energy transfer rate (ϵ_u), large scale energy injection rate ($\int_{1/10km}^{1/100m}\epsilon_f(k)dk$), and small scale energy injection rate ($\int_{1/10km}^{1/100m}\epsilon_f(k)dk$). The values shown are the mean, and the range in the parenthesis are the 5th and 95th percentile.

Quantitative estimates of the upscale energy transfer rate and energy injection rates are summarized in Table 1. The upscale energy transfer rate, the maximum negative value of the spectral flux (Figure 4c,f), and the energy injection at the larger scales, is similar within errorbars between the two seasons. While the energy injected at the smaller scales is enhanced by about 25-30% in the winter. In summer about 75% of the total injected energy, summed over both the large and small scale injections, is transferred upscale, while in winter this ratio is reduced to about 60% - indicating a strengthening of the forward cascade. Note that in both summer

and winter, a fraction of the energy injected at the smaller energy injection scale is transferred upscale. Considering the almost unchanged upscale energy transfer rate (reflective of energy flux to scales greater than 100km), most of the extra energy injected in winter relative to the summer transfers downscale.

The estimation of interscale energy transfers from the observed SF3 indicates that the range of scales from 100m-500km are energized primarily at two distinct scales, which are roughly analogous to the interior deformation radius, O(50km), and the mixed-layer deformation radius, O(1-10km). The energy injection near the mixed-layer deformation radius is seasonally modulated, with the injection rate and scale increasing slightly in winter. This is most likely due to a deepening of the mixed layer, which is in turn associated with more available potential energy for release and a larger scale of instability. About 25-40% of the energy injected into the system cascades to smaller scales, forward cascade, at scales where the Ro>O(1), likely because the flow starts to escape the strong constrain imposed by rotation for energy to be transferred upscale. The flow in the winter has a higher propensity to cascade energy to smaller scales, which may be understood as the more energetic flow in winter having higher speeds and thus a greater likelihood to escape rotational effects. These results provide the first direct estimate of the downscale energy transfer rate, $O(10^{-7}m^2/s^3)$, at the submesoscales. This estimate for the energy transfer rate is similar to those retreived for the energy dissipation in the mixed layer using microstructure estimates (*47*), suggesting that the submesoscale flows can provide a direct pathway towards dissipation.

Discussion

The observations of submesoscale turbulence at the surface ocean, in the Northern Gulf of Mexico, show the presence of a dual energy cascade; energy dominantly cascades towards small-scales at scales smaller than O (1-10 km) and towards large-scales at scales larger than O (1-10

km). The energy injection takes place primarily over two distinct scale ranges, at the smaller scales O(500m-10km) near the mixed-layer deformation radius and at the larger scales O(20-50km) near the interior deformation radius. The presence of a turbulent dual energy cascade has been hypothesised in the literature as a mechanism needed to accomplish the small-scale dissipation in the ocean. Intuitions on its existence stem from high-resolution ocean models and DNS of rotating-stratified flows, but this is the first time it has been directly confirmed in ocean observations using the estimates of third-order structure functions analyzed with an innovative methodology.

The strength of the energy transfers as well as the scales at which the dual cascade develops are modulated seasonally, likely in response to the change in mixed-layer depth and strength of lateral buoyancy gradients set by the atmospheric forcing and freshwater river outflow. The net kinetic energy injection over the observed range of scales and the fraction of this energy cascading forward to smaller scales is enhanced in the winter, when the mixed layer is deeper. Even though the energy injected at small scales increases in the winter, this extra energy injection mainly leads to a strengthening of the downscale flux, without affecting the upscale energy flux at scales larger than 50km. The scale at which the net kinetic energy flux switches from being dominantly towards small-scale to dominantly towards large-scale seems to be correlated with the scale at which the local (in scale) Rossby number becomes O(1), the latter shifting towards larger scales in the winter as the net kinetic in the system increases.

A seasonal modulation in the quasi-equilibrium distribution of kinetic energy over scales is also observed, as evidenced by second-order structure-function analysis and its Helmholtz decomposition. In winter there is more kinetic energy relative to the summer in the flow over the submesoscale range, and also this range of scales is dominantly composed of non-divergent motions. This suggests that the enhancement and changes in flow structures in the winter could likely be tied to a mechanism like mixed-layer instability, which strengthens in the presence

16

of deeper mixed layers and would largely energize the balanced part of the flow. While in the summer, divergent motions make a significant part of the kinetic energy over the submesoscale range, suggesting that the internal waves enhanced in amplitude by the shallower mixed layer or strain-driven ageostrophic frontogenesis are dominant.

Our analysis focused on observations from the Northern Gulf of Mexico, particularly the deeper ocean away from the continental shelf where the seasonal modulation in mixed layer depth is quite large. However, we believe that the presence of a dual energy cascade is likely to be a ubiquitous feature of submesoscale turbulence in the global ocean, and its particular properties, such as the scale at which the net flux changes sign, would be modulated by the local environment. Our results would indicate that if the Ro $> O(1)$ at any scales in a region, then a forward cascade would likely ensue, which is possible as the dynamics would diverge from the traditional quasigeostrophic (QG) phenomenology. This is likely to be true everywhere in the surface ocean, supported based on results from high-resolution numerical simulations, e.g., (*48*), which suggests that the submesoscale range of scales are more energetic than what QG dynamics would suggest in most places, while the particular dynamical contributions to these scales, balanced motions vs internal gravity waves, are modulated seasonally and spatially. It is worth noting that these high-resolution model simulations are far from being converged, and the departure from QG theory is likely to be even more stark as finer scales are resolved and in the real ocean.

This discovery of a well defined dual-energy cascade presented here rests on two key elements: high-density sampling of the surface flows using a dense array of surface drifters (*36,39*), and theoretical advancement in structure-function analysis by generalizing the use of third-order structure functions (*35*). However, as most observational analyses go our results require assumptions and are likely to have some biases that are important to discuss, as they will chart the path for future research. The theory surrounding structure functions is developed in Eule-

rian coordinates and assuming homogeneity and isotropy, while the surface drifters sample the velocity field following the horizontal flow (sampling in a quasi-Lagrangian frame), with the real ocean having some degree of spatial inhomogeneity and anisotropy introduced by the complexity of the domain or forcing mechanisms. It has been shown previously for the GLAD and LASER data that the impacts of inhomogeneity and anisotropy are relatively weak, and do not affect the zeroth-order results (*32, 41*). The quasi-Lagrangian nature of the observations results in biased sampling, as the drifters have a tendency to cluster into convergent regions (*37, 44*). We think that this bias likely results in slightly overestimating the strength of the forward energy cascade at scales smaller than O(1km), as the convergent fronts are likely to be regions where the dissipative processes are stronger (*49*). The exact quantitative impact of these biases remains an open area of research at the moment (*45*), and no methods to systematically correct for their influence are available.

Despite these caveats, direct observational confirmation of the dual energy cascade is a significant step forward in our understanding of how oceanic turbulence operates, and shows that a direct pathway for dissipation of mesoscale kinetic energy is present at the surface ocean. The observational evidence provided here is also relevant from a fundamental standpoint and supports a new paradigm in turbulence, that of a dual energy cascade developing in a fully three-dimensional fluid under the influence of rotation and stratification (*23, 50*). Our results and methods provide therefore important avenues for future research. On the dynamical side, it remains unclear what sets the ratio of the energy that is cascaded downscale vs upscale and how is this ratio seasonally modulated. One possibility is that it might be controlled by the strength of the internal waves, as shown in (*24, 50, 51*), which are more dominant in the summer. A decomposition of the third-order structure functions into contributions from different parts of the flow could be helpful to answer this question. While a pathway for energy dissipation at the surface ocean has been confirmed by the present study, it remains to be understood what the

relative strength of this pathway in dissipating energy and closing the ocean's energy budget is compared to mechanisms that are active in the interior, at land or ice boundaries, or via interaction with surface forcing.

One major advantage of our methodology is that it does not require the observational data sets to be gridded, and can easily handle observations with gaps and non-uniform sampling, which is the case for most observational platforms including satellites. Thus, it is also worth considering how our analysis methods can be expanded to other observational data sets in the future, such as the surface velocities obtained from the Global Drifter Program, measurements that will come from the Surface Water and Ocean Topography satellite, or more targeted observations from process studies where buoyancy measurements are made along with velocity and can allow for consideration of the kinetic and potential energy cycles simultaneously.

Methods

The surface drifters

All the data used in this study was collected by observations from surface drifters, which are instruments that follow the flow in the surface ocean and their locations are tracked using the Global Positioning System (GPS). The location information is then used to infer the surface velocities. The drifters used here tracked the flow in the top 60cm of the surface. Their positions were retrieved at 5min intervals with a nominal position error of < 10m, and these raw position estimates were processed and provided by CARTHE as processed drifter trajectories, which were low pass filtered with a 1hour cutoff and resampled to a uniform time grid of 15 mins. Here we used drifters that were deployed in two targeted studies in the NorthEastern Gulf of Mexico.

The Grand LAgrangian Deployment (GLAD) experiment was conducted in the wake of the Deep Water Horizon oil spill. 297 CODE style surface drifters (*52*) were released over the

period of 11 days at the end of July 2012, making it the largest drifter release experiment at that time (*36*). The trajectories span the period from July to October 2012, which are the summer months.

The LAgrangian Submesoscale ExpeRiment (LASER) was conducted at approximately the same location as GLAD. A total of approximately 1000 surface drifters were released near the end of January 2016, making it the largest drifter deployment to-date. The surface drifters used in LASER, CARTHE style drifters, had a slightly different design than the GLAD drifters, the new design was meant to be more rapidly deployable and also more environmentally friendly (*39*). Despite the design differences the GLAD and LASER drifters showed similar characteristics at following the flow, and for all practical purposes are considered to be the same. The trajectories span the period from January to March 2016, which are the winter months. Many of the LASER drifters lost their drogue at some point after their deployment, and we only use the portion of the trajectories when the drogue was attached (*53*).

The drifters were released in clusters, and so most of the observations at the smallest separation scales ($< 10 days$) are for the duration of late July and early August in GLAD and late January and early February in LASER. The deployments were also often targeted on particular flow features, so the samples at the smallest scales might not be as representative of the true statistics as the samples gathered once the drifters disperse and randomly sample many different flow features.

Statistical metrics and error estimates

The metrics of interest in this study take the general form - $\langle \delta u^n \rangle (r)$, where the $\langle . \rangle$ indicates an ensemble averaging operation, $\delta u(r)$ is the difference in a particular velocity component between two points that are separated by distance r, and this velocity difference is raised to some power of n corresponding to different orders of the structure functions.

20

When estimating these metrics using drifters we assume that the velocity measured by a particular drifter is the velocity of the surface ocean at that location. Using any two drifters we get one sample estimate of $\delta u(r)$. Since we want to estimate the metric as a function of separation scale we divided the separation axis, r, into bins that are logarithmically distributed between 10m and 1000km using the formula $r_n = r_0 \times 1.5^n$, where $r_0 = 10m$ and $n = (0, 1, 2, 3, ...)$. The ensemble averaging is replaced by collecting all pairs in any particular bin and time averaging over the entire duration of the experiment and space averaging, performed by averaging together all the scattered observations being collected by different drifters pairs; this is equivalent to assuming temporal stationarity and spatial homogeneity in a statistical sense. To ensure that the homogeneity assumption is not significantly violated by the samples, we only use pair samples collected by the drifters in a particular region that we expect to have similar dynamics everywhere (Figure SI-1). We also assume isotropy by averaging over all orientations of the position vectors connecting the two drifters relative to the geographical coordinates.

The error estimates on the metrics are calculated by using a form of bootstrapping called modified block bootstrapping. Regular bootstrapping is done by estimating the same statistical metric multiple times by random sampling with replacement, keeping the number of samples the same as the original sample size, from the observed distribution of the samples (the samples for us are measurements of $\delta u(r)^n$ in some separation bin, where the number of samples is smaller than the number of drifter pairs). The mean over these multiple estimates of the metrics is then used as the estimate of the metric, and percentiles of these distributions can be used as estimates of the error - here we use the 5th and 95th percentiles. However, one key assumption in regular bootstrapping is that all the samples are independent, which is not even approximately true for our dataset because of the temporal and spatial correlations between the different pairs. Instead in block bootstrapping the dataset is divided into blocks that are approximately independent, and the resampling is done over these blocks rather than over all the individual samples. Here the

blocks were defined by (a) estimating the total duration (T_{tot}) over which a significant number of data was collected, defined approximately as 90 days during GLAD and 60 days during LASER, (b) estimating the time scale corresponding to each scale ($T_{scale}(r)$), which was estimated as $T_{scale}(r) = r/\sqrt{D_{tot}}$, (c) defining the number of degrees of freedom as $N^{DOF} = T_{tot}/T_{scale}$, and then (d) dividing the total number of samples in each bin (arranged in order with the m individual time series for the m pairs that spent some time in the particular separation bin) into N^{DOF} blocks. This is an approximate but pragmatic procedure, and due to some degree of independence between the different pair time series in each bin actually results in an upper bound on the error bars, since we assume that there are less independent blocks than there actually might be (some independent time series from different pairs might end up in the same block when using our algorithm). This method is described further in section B of the Supp. Info.

2nd order structure functions as proxy for scale-wise kinetic energy distribution

The longitudinal and transverse components of the second-order structure functions are defined as

$$D_{LL}(r) = \left\langle (\delta u_L)^2 \right\rangle, \quad D_{TT}(r) = \left\langle (\delta u_T)^2 \right\rangle \tag{1}$$

where δu_L and δu_T are longitudinal and transverse velocity differences, respectively. These are defined as,

$$\delta u_L = \delta \boldsymbol{u} \cdot \frac{\boldsymbol{r}}{|\boldsymbol{r}|} \quad \text{and} \quad \delta u_T = \delta \boldsymbol{u} \cdot \boldsymbol{t}, \tag{2}$$

where $\boldsymbol{r}$ is the vector connecting the two points ($\boldsymbol{x}_1$ and $\boldsymbol{x}_2$) where simultaneous velocity observations are made ($\boldsymbol{r} = \boldsymbol{x}_2 - \boldsymbol{x}_1$), and $\boldsymbol{t}$ is the unit vector perpendicular to it ($\boldsymbol{r} \cdot \boldsymbol{t} = 0$) on the horizontal plane. $\delta \boldsymbol{u} = \boldsymbol{u}_2 - \boldsymbol{u}_1$ is the difference in velocity between the two points. We refer to the sum of these two components as the total second-order velocity structure function

$(D_{tot} = D_{LL} + D_{TT})$. Plots of these components are presented in the supp info (Figure SI-5).

The second-order structure function is related to the corresponding kinetic energy as an integral relationship, $D_i(r) = \int_0^\infty E_i(k)(1 - J_0(kr))dk$ with $i = LL$ or TT, which is a result of Fourier transformation of isotropic two-dimensional fields. Here $E_i(k)$ is the longitudinal or transverse component of the kinetic energy and $J_0(x)$ is the zeroth-order Bessel function (further discussion of this relationship can be found in (32)). This relationship implies that the SF2 is not precisely related to the kinetic energy at a particular scale, but is rather a weighted version of the kinetic energy distribution. Unfortunately, inverting the relationship to estimate the kinetic energy from the structure function results in an incoherent solution due to amplification of noise, and is therefore not attempted here. However, scalings observed in the second-order structure functions provide a very good measure of the distribution of kinetic energy as a function of scale, and the qualitative conclusions of this paper are robust. We confirm this by using an alternate metric of the distribution of kinetic energy as a function of scale, called the signature function (Supp info. section D), and also by testing the relationship between the structure function and kinetic energy using idealized functional forms with known kinetic distribution (not shown).

The longitudinal and transverse components can be used to infer the rotational (D_R) and divergent (D_D) contributions to SF2, $D_{tot} = D_R + D_D$, using a Helmholtz decomposition (42, 43). This is performed by using the following formulae,

$$D_R(r) = D_{TT}(r) + \int_0^\infty \frac{1}{r}(D_{TT}(r) - D_{LL}(r))dr \tag{3}$$

$$D_D(r) = D_{LL}(r) - \int_0^\infty \frac{1}{r}(D_{TT}(r) - D_{LL}(r))dr \tag{4}$$

The rotational and divergent estimates are more useful as they are closely related to different dynamical regimes, where balanced vortical flows are primarily rotational in nature while ageostrohic flows or internal waves have a significant contribution from the divergent part.

These formulae are derived under assumptions of isotropy and homogeneity. When these assumptions are not perfectly satisfied, the estimates can have some nonphysical characteristics: In particular, at scales where one component (rotational or divergent) is significantly smaller than the other, the formulae can result in negative values for the second-order velocity structure functions (shown in Figure SI-6, and can be seen as a range of scales where $SF2_D$ is not plotted in Figure 2). Some corrections can be introduced to account for factors like anisotropy, e.g. (*41*), but were not used here because for the particular datasets under consideration adding complexity would not impact the qualitative conclusions.

3rd order structure functions and inter-scale energy transfers

The 3rd order velocity structure function (SF3 or V), defined as,

$$V = \left\langle \delta u_L \left(\delta u_L^2 + \delta u_T^2 \right) \right\rangle, \tag{5}$$

is related to the spectral flux ($F(k)$) through a Fourier transform as,

$$V(r) = -4r \int_0^\infty \frac{1}{k} F(k) J_2(kr) dk, \tag{6}$$

where $J_2(x)$ is the second-order Bessel function.

Here we discretize $F(k)$ using a set of piecewise constant basis,

$$F(k) = -\epsilon_u + \sum_{j=1}^{N_f} \epsilon_j H(k - k_j) dk_j, \tag{7}$$

where ϵ_u is the upscale energy transfer rate (units L^2/T^3), ϵ_j is the energy injection density (energy injection per unit wavenumber, units L/T^3) at wavenumber k_j. The total energy input into the system would be $\sum_j \epsilon_j dk_j$, and this sum can be done over a fixed range of scales to estimate the energy input or injection (units L^2/T^3) at those scales (as done for Table 1).

Substituting (7) into (6), we obtain

$$V(r) = 2\epsilon_u r - \sum_{j=1}^{N_f} 4 \frac{\epsilon_j}{k_j} J_1(rk_j) dk_j, \tag{8}$$

which links the measurable third-order structure function with physically important quantities including the energy injection rates at different scales and the largest-scale upscale energy transfer rate.

Now, we estimate $V(r)$ from surface drifter data, and fit the structure function using (25) to obtain ϵ_u and ϵ_j, which are then be used to gain insights into the kinetic energy transfer across scales, e.g., by calculating the corresponding $F(k)$ using (7). Here we fit the estimated $V(r)$ over the range of scales from 50m-500km, to avoid scales where the estimates of $V(r)$ are less certain. However, the exact choice of this range did not impact the results of our study. The details of this estimation problem (inverse problem) and the relationship between the spectral flux and SF3 are discussed in the supp info section F.

References

1. R. Ferrari, C. Wunsch, Ocean circulation kinetic energy: Reservoirs, sources, and sinks, *Annual Review of Fluid Mechanics* **41** (2009).

2. R. Tulloch, J. Marshall, C. Hill, K. S. Smith, Scales, growth rates, and spectral fluxes of baroclinic instability in the ocean, *Journal of Physical Oceanography* **41**, 1057 (2011).

3. R. Salmon, Two-layer quasi-geostrophic turbulence in a simple special case, *Geophysical & Astrophysical Fluid Dynamics* **10**, 25 (1982).

4. G. K. Vallis, *Atmospheric and oceanic fluid dynamics* (Cambridge University Press, 2017).

5. C. Wunsch, R. Ferrari, Vertical mixing, energy, and the eneral circulation of the oceans., *Annu. Rev. Fluid Mech.* **36**, 281 (2004).

6. J. Callies, R. Ferrari, O. Bühler, Transition from geostrophic turbulence to inertia-gravity waves in the atmospheric energy spectrum, *Proc. Nat. Acad. Sciences* **111.48**, 17033 (2014).

7. C. B. Rocha, T. K. Chereskin, S. T. Gille, D. Menemenlis, Mesoscale to submesoscale wavenumber spectra in drake passage, *Journal of Physical Oceanography* **46**, 601 (2016).

8. H. Sasaki, P. Klein, B. Qiu, Y. Sasai, Impact of oceanic-scale interactions on the seasonal modulation of ocean dynamics by the atmosphere, *Nature communications* **5**, 1 (2014).

9. J. Callies, R. Ferrari, J. M. Klymak, J. Gula, Seasonality in submesoscale turbulence, *Nature communications* **6**, 1 (2015).

10. C. E. Buckingham, *et al.*, Seasonality of submesoscale flows in the ocean surface boundary layer, *Geophysical Research Letters* **43**, 2118 (2016).

11. J. Zhang, *et al.*, Seasonal modulation of submesoscale kinetic energy in the upper ocean of the northeastern south china sea., *Journal of Geophysical Research: Oceans* **126**, e2021JC017695 (2021).

12. G. Lapeyre, P. Klein, Dynamics of the upper oceanic layers in terms of surface quasi-geostrophy theory., *J. Phys. Oceanogr* **36**, 165 (2006).

13. G. Roullet, J. C. McWilliams, X. Capet, M. Molemaker, Properties of steady geostrophic turbulence with isopycnal outcropping., *J. Phys. Oceanogr* **42**, 18 (2012).

14. G. Boccaletti, R. Ferrari, B. Fox-Kemper, Mixed layer instabilities and restratification., *J. Phys. Oceanogr* **37**, 2228 (2007).

15. J. Callies, O. Bühler, R. Ferrari, The dynamics of mesoscale winds in the upper troposphere and lower stratosphere, *J. Atmos. Sci.* **73**, 4853 (2016).

16. J. C. McWilliams, Submesoscale currents in the ocean, *Proceedings of the Royal Society A: Mathematical, Physical and Engineering Sciences* **472**, 20160117 (2016).

17. P. Klein, *et al.*, Ocean-scale interactions from space, *Earth and Space Science* **6**, 795 (2019).

18. Z. Su, J. Wang, P. Klein, A. F. Thompson, D. Menemenlis, Ocean submesoscales as a key component of the global heat budget, *Nature communications* **9**, 1 (2018).

19. D. Balwada, K. S. Smith, R. Abernathey, Submesoscale vertical velocities enhance tracer subduction in an idealized antarctic circumpolar current, *Geophysical Research Letters* **45**, 9790 (2018).

20. T. Uchida, *et al.*, The contribution of submesoscale over mesoscale eddy iron transport in the open southern ocean, *Journal of Advances in Modeling Earth Systems* **11**, 3934 (2019).

21. X. Capet, J. C. McWilliams, M. J. Molemaker, A. F. Shchepetkin, Mesoscale to submesoscale transition in the california current system. part iii: Energy balance and flux, *Journal of Physical Oceanography* **38**, 2256 (2008).

22. Y. Yang, *et al.*, Spatial and temporal characteristics of the submesoscale energetics in the gulf of mexico, *Journal of Physical Oceanography* (2020).

23. A. Pouquet, R. Marino, P. D. Mininni, D. Rosenberg, Dual constant-flux energy cascades to both large scales and small scales, *Phys. Rev. Fluids* **29**, 111108 (2017).

24. R. Marino, P. D. Mininni, D. Rosenberg, A. Pouquet, Inverse cascades in rotating stratified turbulence: Fast growth of large scales, *Europhysics letters* **102**, 44006 (2013).

25. U. Frisch, *Turbulence: the legacy of A. N. Kolmogorov* (Cambridge university press, 1995).

26. R. B. Scott, F. Wang, Direct evidence of an oceanic inverse kinetic energy cascade from satellite altimetry, *J. Phys. Oceanogr.* **35**, 1650 (2005).

27. H. Khatri, J. Sukhatme, A. Kumar, M. K. Verma, Surface ocean enstrophy, kinetic energy fluxes, and spectra from satellite altimetry, *Journal of Geophysical Research: Oceans* **123**, 3875 (2018).

28. H. Aluie, M. Hecht, G. K. Vallis, Mapping the energy cascade in the north atlantic ocean: The coarse-graining approach, *J. Phys. Oceanogr.* **48**, 225 (2018).

29. J. Harlan, *et al.*, The integrated ocean observing system high-frequency radar network: status and local, regional, and national applications, *Marine Technology Society Journal* **44**, 122 (2010).

30. A. C. N. Garabato, *et al.*, Kinetic energy transfers between mesoscale and submesoscale motions in the open ocean's upper layers, *Journal of Physical Oceanography* **52**, 75 (2022).

31. J. Y. N. Cho, E. Lindborg, Horizontal velocity structure functions in the upper troposphere and lower stratosphere 1. Observations, *Journal of Geophysical Research* **106**, 10223 (2001).

32. D. Balwada, J. H. LaCasce, K. G. Speer, Scale-dependent distribution of kinetic energy from surface drifters in the gulf of mexico, *Geophys. Res. Lett.* **43**, 10856 (2016).

33. A. C. Poje, T. M. Özgökmen, D. J. Bogucki, A. Kirwan, Evidence of a forward energy cascade and kolmogorov self-similarity in submesoscale ocean surface drifter observations, *Physics of Fluids* **29**, 020701 (2017).

34. M. Berta, *et al.*, Submesoscale kinematic properties in summer and winter surface flows in the northern gulf of mexico, *Journal of Geophysical Research: Oceans* **125**, e2020JC016085 (2020).

35. J.-H. Xie, O. Bühler, Third-order structure functions for isotropic turbulence with bidirectional energy transfer, *J. Fluid. Mech.* **877**, R3 (2019).

36. A. C. Poje, *et al.*, Submesoscale dispersion in the vicinity of the deepwater horizon spill, *Proceedings of the National Academy of Sciences* **111**, 12693 (2014).

37. E. A. D'Asaro, *et al.*, Ocean convergence and the dispersion of flotsam, *Proceedings of the National Academy of Sciences* **115**, 1162 (2018).

38. R. Barkan, *et al.*, Submesoscale dynamics in the northern gulf of mexico. part i: Regional and seasonal characterization and the role of river outflow, *Journal of Physical Oceanography* **47**, 2325 (2017).

39. G. Novelli, *et al.*, A biodegradable surface drifter for ocean sampling on a massive scale, *Journal of Atmospheric and Oceanic Technology* **34**, 2509 (2017).

40. E. A. D'Asaro, Mixed layer velocities induced by internal waves, *Journal of Geophysical Research: Oceans* **83**, 2437 (1978).

41. H. Wang, O. Bühler, Anisotropic statistics of lagrangian structure functions and helmholtz decomposition, *Journal of Physical Oceanography* **51**, 1375 (2021).

42. E. Lindborg, A helmholtz decomposition of structure functions and spectra calculated from aircraft data, *J. Fluid Mech.* **762**, R4 (2015).

43. O. Bühler, J. Callies, R. Ferrari, Wave-vortex decomposition of one-dimensional ship-track data, *J. Fluid Mech.* **756**, 1007 (2014).

44. J. Pearson, *et al.*, Impacts of convergence on structure functions from surface drifters in the gulf of mexico, *Journal of Physical Oceanography* **49**, 675 (2019).

45. J. Pearson, *et al.*, Biases in structure functions from observations of submesoscale flows, *Journal of Geophysical Research: Oceans* **125**, e2019JC015769 (2020).

46. A. N. Kolmogorov, *Dokl. Akad. Nauk SSSR* (1941), vol. 32, pp. 16–18.

47. J. Moum, W. Smyth, Upper ocean mixing, *Encyclopedia of Ocean Sciences* **6**, 3093 (2001).

48. H. S. Torres, *et al.*, Partitioning ocean motions into balanced motions and internal gravity waves: A modeling study in anticipation of future space missions, *Journal of Geophysical Research: Oceans* **123**, 8084 (2018).

49. E. D'asaro, C. Lee, L. Rainville, R. Harcourt, L. Thomas, Enhanced turbulence and energy dissipation at ocean fronts, *science* **332**, 318 (2011).

50. R. Marino, A. Pouquet, D. Rosenberg, Resolving the paradox of oceanic large-scale balance and small-scale mixing, *Phys. Rev. Lett.* **114**, 114504 (2015).

51. J.-H. Xie, Downscale transfer of quasigeostrophic energy catalyzed by near-inertial waves, *J. Fluid Mech.* **904**, A40 (2020).

52. R. Lumpkin, T. Özgökmen, L. Centurioni, Advances in the application of surface drifters, *Annual Review of Marine Science* **9**, 59 (2017).

53. A. C. Haza, *et al.*, Drogue-loss detection for surface drifters during the lagrangian submesoscale experiment (laser), *Journal of Atmospheric and Oceanic Technology* **35**, 705 (2018).

54. P. A. Davidson, *Turbulence: an introduction for scientists and engineers* (Oxford university press, 2015).

55. P. G. Saffman, D. I. Pullin, Calculation of velocity structure functions for vortex models of isotropic turbulence, *Phys. Fluids* **8**, 3072 (1996).

56. Q. Nie, S. Tanveer, A note on third-order structure functions in turbulence., *Proc. R. Soc. Lond. A* **455**, 1615 (1999).

57. C. M. Casciola, P. Gualtieri, R. Benzi, R. Piva, Scale-by-scale budget and similarity laws for shear turbulence, *J. Fluid Mech.* **476**, 105 (2003).

58. M. Wan, S. Servidio, S. Oughton, W. H. Matthaeus, The third-order law for increments in magnetohydrodynamic turbulence with constant shear, *Phys. Plasmas* **16**, 090703 (2009).

Acknowledgments

All the codes for the analysis and figure generation are available at

`https://github.com/dhruvbalwada/SF3_to_KEflux.`

Supplementary Information

A   GLAD and LASER data distribution

Figure SI-1 shows the distribution of data as a function of separation scale, time, and spatial location. A subset of the full data set (Figure 2) was chosen for the analysis, in region defined by 91W to 84W, North of 24N, and in ocean deeper than 500m, to ensure near homogeneity and similar dynamics over the samples. Lot of drifters during the LASER experiment lost their drogues, which leads to a rapid decrease of observed pairs in Figure SI-1e, even though approximately 3 times as many drifters as the GLAD experiment were deployed.
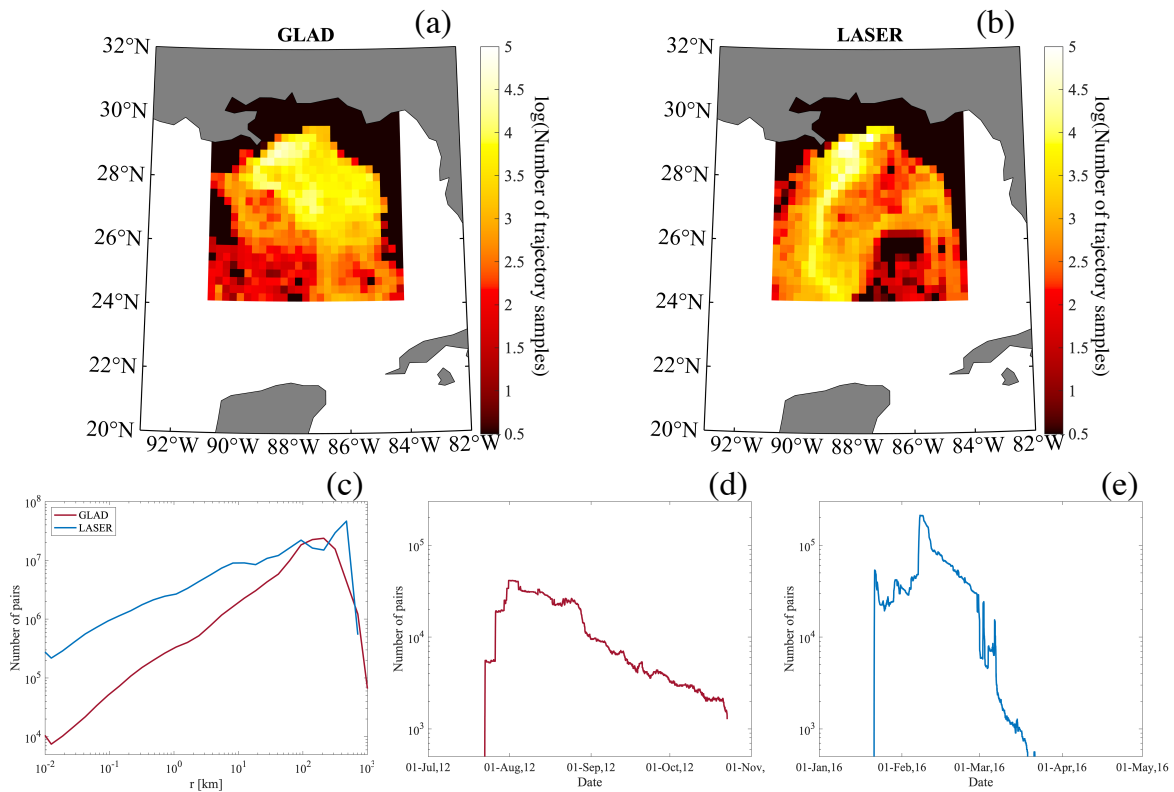

Figure SI-1: **Data distribution** (a,b) Number of trajectory samples in $0.25^o \times 0.25^o$ bins over the region that was used for the analysis (91W to 84W, North of 24N, and in ocean deeper than 500m), (c) number of pairs as per separation, (d, e) number of pairs as a function of time for GLAD and LASER respectively.

B Error Estimates - Modified Block Bootstrapping

In this work we need to estimate errors on different statistical metrics that are all estimates of the mean, albeit of a complex looking statistic $\delta u(r)^n$. Thus a method to estimate errors on the sample mean is needed. However, estimating this errors is non-trivial. Part of the reason for this complexity is that no analytical form is known for the sample distribution (distribution of δu^n, Figure SI-2), and so no standard formula for error is available. An alternative error estimation technique is bootstrapping (`https://en.wikipedia.org/wiki/Bootstrapping_(statistics)`), which involves random resampling with repetitions from the available data samples (mimicking the sampling process) and estimating the means using these randomly generated datasets. The distribution of these estimated means can then be used to infer the errorbars or the confidence intervals.
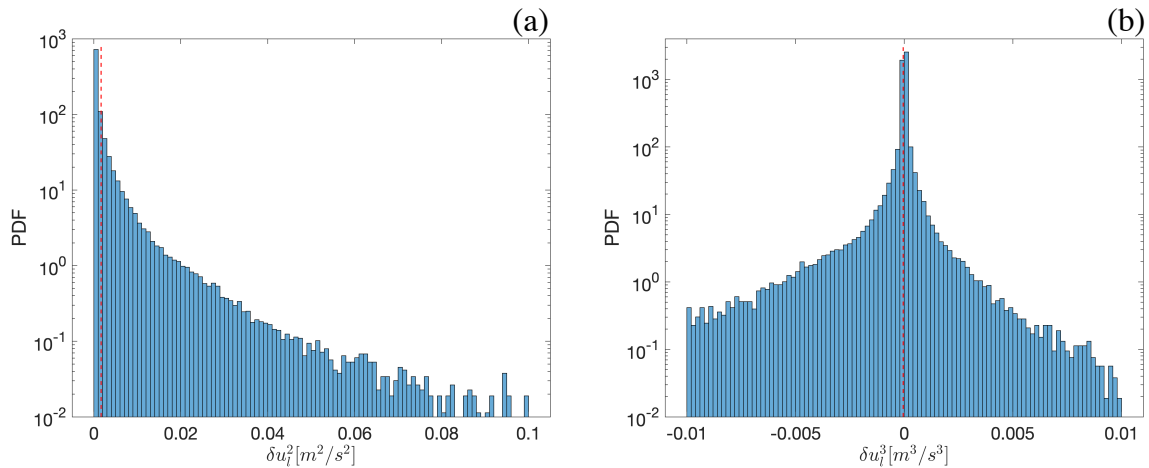

Figure SI-2: Distribution of $\delta u^2(r)$ (a) and $\delta u^3(r)$ for the GLAD experiment for the bin between 577 and 865m. The sample means are shown as the vertical red lines.

This standard bootstrapping technique is not appropriate for us because it assumes that all available samples are independent, which is not the case here. Our samples are collected by pairs of surface drifters that are within a separation distance belonging to a finite-sized separation bin. Since the drifter pair can potentially stay in a particular bin for a finite amount of time,

particularly in the larger bins at greater separations, we get a time series that will have some temporal correlation between samples (Figure SI-3). Additionally, if two or more pairs are in close proximity to each other and sampling the same flow feature the samples collected by the different pairs will also have some spatial correlation. The Lagrangian nature of the sampling mixes these temporal and spatial correlations.
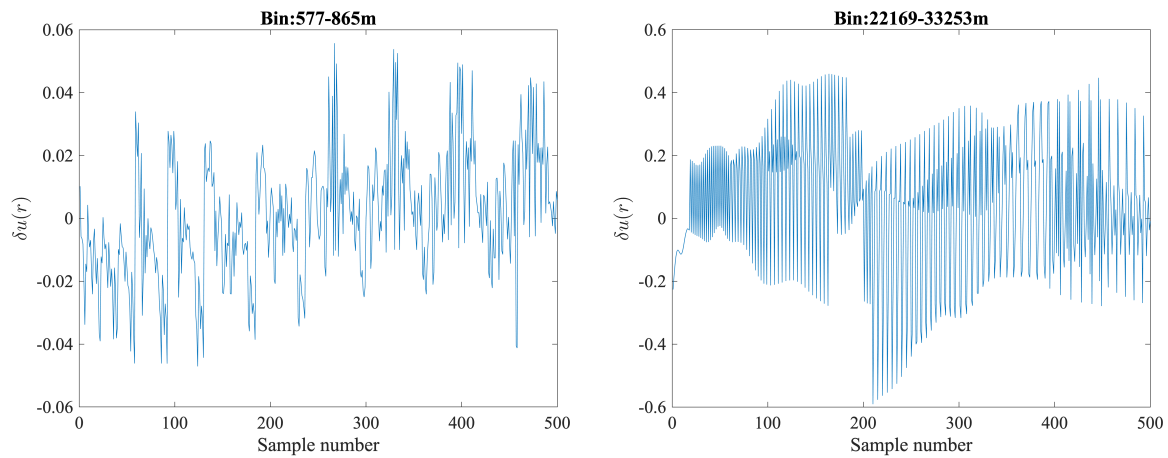

Figure SI-3: $deltau$ obtained from samples in two different separation bins - showing temporal coherence, and hence a lack of independence between samples.

Since the samples are correlated we looked towards *block bootstrapping*. This technique is usually used with time-series data, where the total time series is first divided into blocks based on some temporal correlation scale. For example, if the correlation scale is 10 days and the time series is 100 days long we would divide the timeseries into ten 10 day blocks. The resampling is then done using these blocks as individual samples. Here we do not have a single time series but rather a concatenated time series made up of different pairs that belong in a separation bin (Figure SI-3), where the different pairs are also likely to be correlated due to spatial proximity – particularly at large-separation scales that are accounting for larger flow features that evolve slowly. Thus, using the traditional block bootstrapping also does not work for us; we experimented with this and found the error estimates to be intuitively too small (not
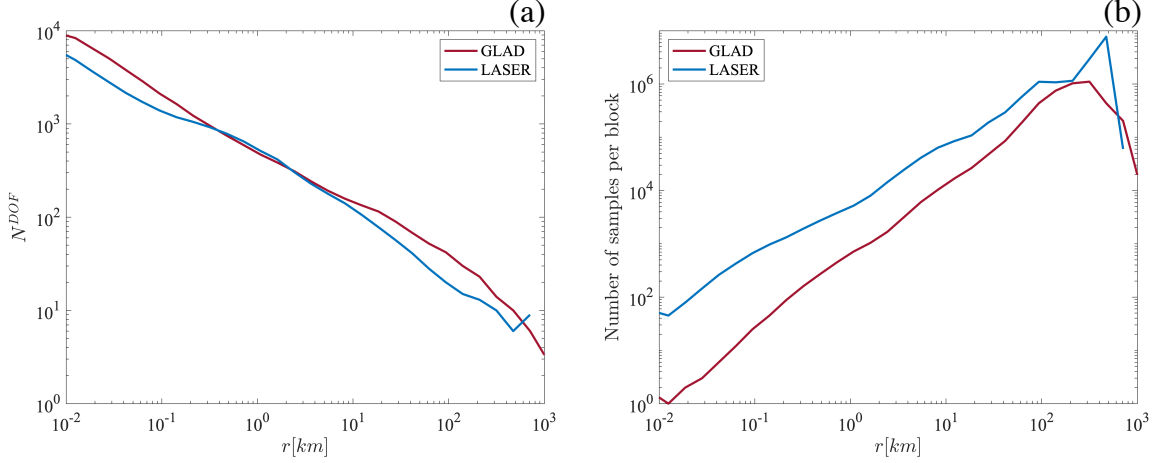
35

shown).

Figure SI-4: (a) Number of degrees of freedom (same as number of blocks) as a function of separation scale, and (b) number of samples per block as a function of separation scale.

Instead we use a slightly modified version of the block bootstrapping. We first estimate the possible degrees of freedom for any particular separation bin based on a temporal correlation scale and the total duration of the experiment. The temporal correlation scale was estimated using the estimate of the total SF2, as $T_{scale}(r) = r/\sqrt{D_{tot}(r)}$. The duration of the experiment, T_{total} was chosen as roughly the duration over which a large number of pairs are present, and was chosen as 90 days for GLAD and 60 days for LASER (Figure SI-1d,e). Then the number of degrees of freedom was defined as $N^{DOF}(r) = T_{total}/T_{scale}(r)$, and is shown in Figure SI-4 for the two experiments. As one might expect the $N^{DOF}(r)$ decreases as a function of scale, since fewer independent large-scale events are sampled. Then we took the concatenated set of samples for any separation bin and divided them into $N_{DOF}(r)$ blocks, and used these blocks as independent samples for block bootstrapping. Our underestimate of $N_{DOF}(r)$ is most likely smaller than the actually degrees of freedom (which is unknown), since we are not accounting for the fact that some samples might be uncorrelated because of large spatial separation, and is likely to give an upper bound on the error estimates. Our approach to estimating the blocks

and consequently the errors is approximate but pragmatic, and we hope that future work can develop more precise error estimates.

C Additional plots of Second-Order Structure Functions

Figure SI-5 shows the two raw components, longitudinal and transverse, of the total SF2 and figure SI-6 shows the two decomposed components, rotational and divergent, of the total SF2. The information in figure SI-6 is the same as figure 2, and is shown on a linear axis so that the negative values can be seen. In principle all the components of the SF2 should be positive, but the divergent components takes negative values over some range of scales. These negative values are small compared to the rotational or total components, about 20% at maximum but usually much smaller contribution to the total. This non-physical result is likely because the assumptions required to derive the structure function decomposition formulae (equation 3 and 4) are not perfectly satisfied, and this failure in the method has been discussed in length in (*41*).
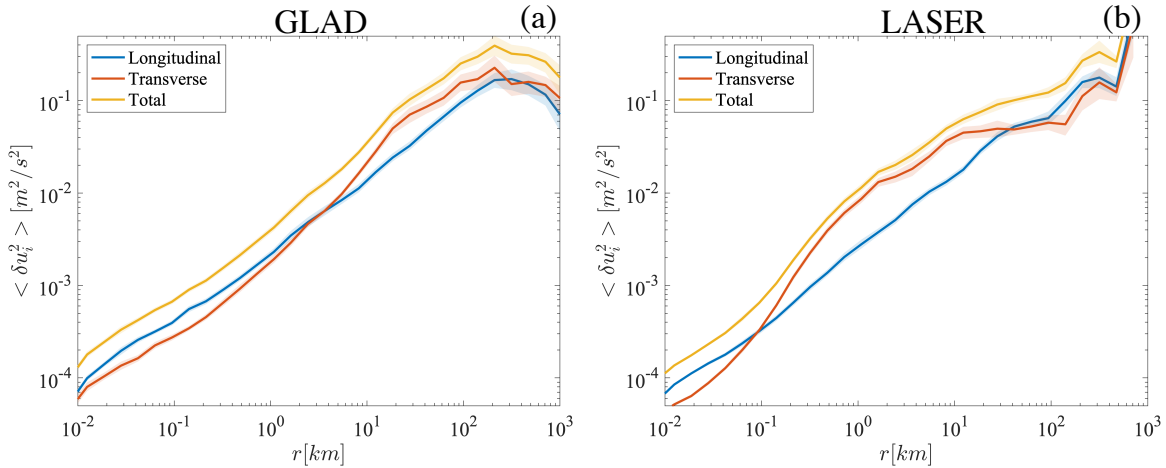

Figure SI-5: Longitudinal (D_{LL}) and transverse (D_{TT}) components of SF2 for the (a) GLAD and (b) LASER experiments.
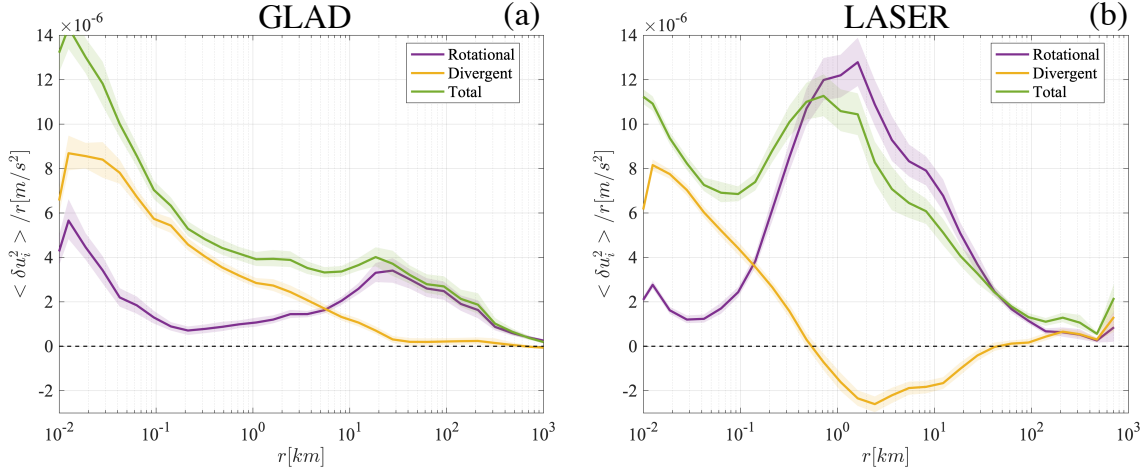
Figure SI-6: Rotational (D_R) and divergent (D_R) components of SF2 for the (a) GLAD and (b) LASER experiments compensated by r for visualization purpose on a linear axis.

D   Signature functions - an alternate metric for distributions of kinetic energy as a function of scale

Second-order structure functions (SF2) represent a smoothed version of the distribution of kinetic energy across scales. This is because at any scale the SF2 includes a sum of energy from all smaller scales, but also enstrophy from all larger scales (which is often small as enstrophy is usually cascading downscale). (*54*) proposed signature function as an alternative function that is better representative of the kinetic energy at different scales, and can be almost be considered comparable to the kinetic energy spectrum. It is defined as,

$$G(r) = -\frac{r^2}{4}\frac{\partial}{\partial r}\left(\frac{1}{r}\frac{\partial}{\partial r}\left\langle \delta u^2 \right\rangle\right). \tag{9}$$

One caveat of the signature function when working with observational estimates is the requirement to estimate derivatives. Here we ameliorate the noisy nature of derivatives by fitting a 5th-order polynomial to the SF2 before estimating the signature function (the results here are not overly sensitive to this choice).

The signature function estimates are shown in Figure SI-7. While there are some quantita-
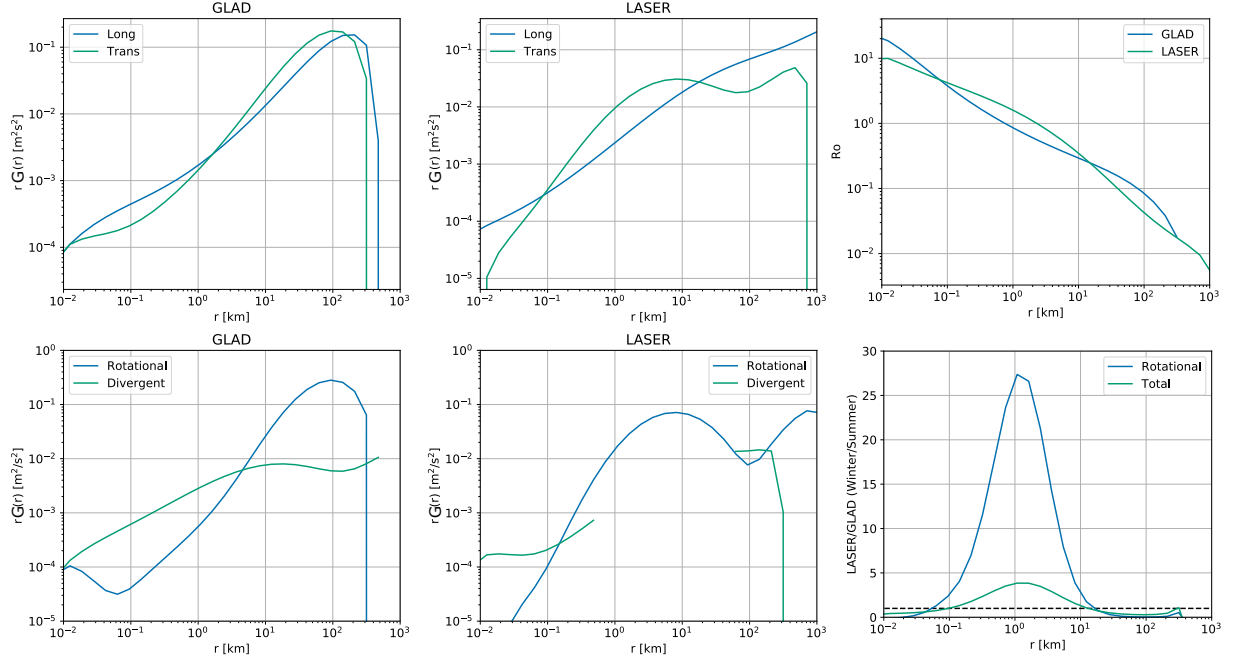
38

Figure SI-7: **Signature functions for the GLAD and LASER experiment.** (a, b) The longitudinal and transverse components. (c) the Rossby number for the two experiments. (d, e) The rotational and divergent decomposition. (f) The ratio of the total and rotational components between the two experiments.

tive differences compared to the SF2, in part due to the polynomial fitting, none of the major qualitative results about the relative behavior of winter vs summer or rotational vs divergent flows change. Part of the reason for this is that most of the enstrophy the type of flows we are considering is expected to be at the smaller scales, and so the SF2 is a good metric to express the distribution of KE across scales.

E   Details of the third-order structure-function theory

Here we first discuss the derivation of the Karman-Howarth-Monin (KHM) equation in our context, and then discuss the relationship between the third-order structure function and the spectral flux.

E.1 Derivation of the KHM equation

The goal of the theory is to describe the dynamics influencing the horizontal velocity correlations, and how the non-linear interactions leading to cross-scale energy transfers can be quantified by using the 3rd-order velocity structure functions. We focus on horizontal kinetic energy (KE), since in the ocean at the scales of interest the the horizontal kinetic energy is the dominant reservoir of KE, and also because the drifters only track the horizontal flow.

We consider the f-plane horizontal momentum equation,

$$\boldsymbol{u}_t + \nabla \cdot (\boldsymbol{u}\boldsymbol{u}) + \partial_z (w\boldsymbol{u}) + f\boldsymbol{u}^\perp = -\nabla p + \boldsymbol{F} + \boldsymbol{D}, \tag{10}$$

where $\boldsymbol{u} = (u, v)$ is the horizontal velocity, $\boldsymbol{u}^\perp = (-v, u)$, w is the vertical velocity, $\nabla = (\partial_x, \partial_y)$ is the horizontal gradient, f is the Coriolis frequency, p is the pressure, $\boldsymbol{F}$ is an external force, and $\boldsymbol{D}$ denotes the dissipation. The dissipation term can contain both large- and small-scale dissipation.

To derive expressions for quantities that can be estimated using horizontal movement of drifters, we next consider two-point correlations with horizontal displacements. We denote the horizontal locations of two points as $\boldsymbol{x}_1$ and $\boldsymbol{x}_2$, respectively, and $\boldsymbol{r} = \boldsymbol{x}_2 - \boldsymbol{x}_1$ is the horizontal displacement vector between these two points. Thus, we define the velocity at location $\boldsymbol{x}_i$ as $\boldsymbol{u}_i$, and the velocity difference is defined as

$$\delta\boldsymbol{u} = \boldsymbol{u}_2 - \boldsymbol{u}_1. \tag{11}$$

By assuming *horizontal homogeneity* we obtain the following relation between the spatial derivatives (*25*),

$$\nabla \equiv \nabla_{\boldsymbol{r}} = \nabla_{\boldsymbol{x}_2} = -\nabla_{\boldsymbol{x}_1}. \tag{12}$$

Homogeneity also results in the statistics of velocity difference to only be a function of the displacement. e.g.

$$\overline{\delta\boldsymbol{u}^2}(\boldsymbol{x}_1, \boldsymbol{x}_2) = \overline{\delta\boldsymbol{u}^2}(\boldsymbol{r}), \tag{13}$$

40

where the $\overline{(.)}$ denotes an ensemble average. Practically the ensemble average is approximated by a time and space average over all drifter pairs (discussed in "Statistical metrics and error estimates" in the Methods). The assumption of homogeneity is foremost a pragmatic one, since it allows us to average over the full data set to ensure robust statistics.

Multiplying $\boldsymbol{u}_1$ to the momentum equation (10) evaluated at $\boldsymbol{x}_2$, adding the conjugate equation, and then assuming a statistically steady state, we obtain the steady Karman-Howarth-Monin (KHM) equation (*25*),

$$-\frac{1}{4}\nabla \cdot \boldsymbol{V} = P + D, \tag{14}$$

where

$$\boldsymbol{V} = \overline{\delta\boldsymbol{u}|\delta\boldsymbol{u}|^2}, \tag{15a}$$

$$P = \frac{1}{4}\nabla \cdot \left(\overline{\boldsymbol{u}_2|\boldsymbol{u}_1|^2} - \overline{\boldsymbol{u}_1|\boldsymbol{u}_2|^2}\right) - \frac{1}{2}\left(\overline{\boldsymbol{u}_1 \cdot \partial_z (w_2\boldsymbol{u}_2)} + \overline{\boldsymbol{u}_2 \cdot \partial_z (w_1\boldsymbol{u}_1)}\right)$$
$$+ \frac{1}{2}\nabla \cdot \left(\overline{\boldsymbol{u}_2 p_1} - \overline{\boldsymbol{u}_1 p_2}\right) + \frac{1}{2}\left(\overline{\boldsymbol{u}_1 \cdot \boldsymbol{F}_2} + \overline{\boldsymbol{u}_2 \cdot \boldsymbol{F}_1}\right) \tag{15b}$$

$$D = \frac{1}{2}\left(\overline{\boldsymbol{u}_1 \cdot \boldsymbol{D}_2} + \overline{\boldsymbol{u}_2 \cdot \boldsymbol{D}_1}\right). \tag{15c}$$

$\boldsymbol{V}$ is the 3rd-order structure-function vector. P subsumes terms corresponding to nonzero horizontal divergence, vertical velocity effect, pressure gradient and the external-forcing. D is the effect of dissipation.

If we further assume hydrostatic balance in the vertical and vertical homogeneity we can express the pressure-related term in (15b) through buoyancy θ as

$$\nabla \cdot \left(\overline{\boldsymbol{u}_2 p_1} - \overline{\boldsymbol{u}_1 p_2}\right) = \overline{w_1\theta_2} + \overline{w_2\theta_1}, \tag{16}$$

which corresponds to conversion between potential and kinetic energy through processes such as baroclinic instability.

Further, we also assume *isotropy*. (*32, 41*) showed that isotropy is not strictly valid for the datasets under consideration, but it serves as a pragmatic assumption. Also, we average mea-

41

sured structure functions in different directions with the same two-point distance (r), which is equivalent to an azimuthal/angle average that removes the dependence on orientation or angle (*55–58*). If the displacements of two measured points are uniformly distributed, this average procedure keeps the isotropic components and therefore the isotropic theory works. Nuances associated with the assumptions of homogeneity and isotropy can be explored in future work.

Thus,

$$\boldsymbol{V} = V(r)\boldsymbol{e}_r, \tag{17}$$

where $\boldsymbol{e}_r = (x/r,\, y/r)$ with $r = \sqrt{x^2 + y^2}$ and $\boldsymbol{e}_r$ is an unit vector. We can estimate V directly from the velocity measured by the drifters,

$$V = \overline{\delta u_L \left(\delta u_L^2 + \delta u_T^2\right)}, \tag{18}$$

where δu_L and δu_T are longitudinal and transversal velocity differences, respectively. And they are defined as

$$\delta u_L = \delta\boldsymbol{u} \cdot \frac{\boldsymbol{r}}{|\boldsymbol{r}|} \quad \text{and} \quad \delta u_T = \delta\boldsymbol{u} \cdot \boldsymbol{t}, \tag{19}$$

where the unit vector $\boldsymbol{t}$ satisfies $\boldsymbol{t} \cdot \boldsymbol{r} = 0$ and $\boldsymbol{r} \times \boldsymbol{t} = \boldsymbol{z}$ with $\boldsymbol{z}$ the vertical unit vector.

E.2 Relationship between the third-order structure function and spectral flux

We showed above that the the SF3 or $V(r)$ is present as a term in the KHM equation, which describes the dynamics of two-point velocity correlations. An analogous equation to the KHM equation can also be derived in spectral space, which describes the dynamics of the velocity power spectra (*25*).

Note that the two-point correlation and power spectra are related via a Fourier transform. Thus, the third-order structure function can be related to the spectral flux via an integral rela-

tionship,

$$V(r) = -4r \int_0^\infty \frac{1}{K} F(K) J_2(Kr) dK, \tag{20}$$

where J_2 is the second-order Bessel function. The Bessel function emerges from a Fourier transform due to the assumption of isotropy (*35*).

Case of a single injection scale

A common ideal scenario that is considered in turbulence theories is an energy injection at a single forcing scale, which corresponds to the spectral flux

$$F(K) = -\epsilon_u + \epsilon H(K - k_f), \tag{21}$$

where ϵ_u is the energy flux upscale and ϵ is the energy injection at the scale corresponding to k_f. This expression assumes that some fraction of the injected energy is fluxed upscale and the rest downscale, here the magnitude of downscale energy flux is $\epsilon_d = \epsilon - \epsilon_u$. This is regarded as an ideal case as the dissipation only happens at zero and infinite wavenumbers.

Substituting (21) into (20) results in the corresponding expression of the third-order structure function (*35*):

$$V = 2\epsilon_u r - 4\epsilon k_f J_1(k_f r), \tag{22}$$

where J_1 is the Bessel function of the first order.

Expression (22) has three power-law ranges, corresponding to the inertial ranges of upscale energy transfer, downscale energy transfer and downscale enstrophy transfer, respectively. These ranges are shown in the asymptotic expansions as follows

$$V = \begin{cases} \underbrace{-2\epsilon_d r}_{\text{downscale energy}} + \underbrace{\frac{1}{4}\left(\frac{r}{l_f}\right)^2 \epsilon r}_{\text{"enstrophy"}} + O\left(\left(\frac{r}{l_f}\right)^5\right), & \text{when} \quad \frac{r}{l_f} \ll 1, \\[3em] \underbrace{2\epsilon_u r}_{\text{upscale energy}} + O\left(\left(\frac{r}{l_f}\right)^{-1/2}\right), & \text{when} \quad \frac{r}{l_f} \gg 1. \end{cases} \tag{23}$$

43

By capturing the three inertial ranges in one formula with resolved forcing scale and with the applicability to the scenario of bidirectional energy transfer, expression (22) solves shortcomings of the previous theories which are only applicable to inertial ranges with unidirectional energy transfer, and therefore it provides the foundation of analyzing third-order structure function measured in geophysical turbulence. Another advantage of the new theory is that it can be used to detect the energy injection scales and the magnitude of energy injection at each scale, which was not possible using classic inertial-range theories because inertial range by definition is away from the forcing scales.

F   Details of parameter estimation method

F.1   Formulation of the discrete problem

Gaining inspiration from equation 21, we can express any general form of the spectral flux as

$$F(k) = -\epsilon_u + \sum_{j=1}^{N_f} \epsilon_j H(k - k_j) dk_j, \tag{24}$$

where ϵ_u is the upscale energy transfer rate (units L^2/T^3), ϵ_j is the energy injection density at scale k_j (energy injection per unit wavenumber, units L/T^3). Note that we indexed dk_j to denote that the forcing wavenumber spacing does not need to be regular. This equation is a discrete representation of the true spectral flux using a set of piece-wise constant basis function.

This equation above can then be passed through the same procedure as what was done for the single forcing scale (equation 22), to derive the corresponding expression for the 3rd-order structure function (V),

$$V(r) = 2\epsilon_u r - \sum_{j=1}^{N_f} 4\frac{\epsilon_j}{k_j} J_1(rk_j) dk_j. \tag{25}$$

We will fit the observational estimate of SF3 using this expression to estimate the parameters, and hence obtain an estimate of the corresponding spectral flux. We do not directly use (6) to

obtain energy flux from the observed third-order structure functions to avoid the amplification of small-scale error in the inverse problem.

The V is estimated at discrete scales r_i with $i = 1, 2, ..., N_r$, which are set based on the used binning. Thus, we obtain a linear equation for ϵ_u and $\epsilon_j (= \epsilon_f(k_j))$,

$$
\begin{bmatrix} V(r_1) \\ V(r_2) \\ ... \\ V(r_{N_r}) \end{bmatrix} = \begin{bmatrix} 2r_1 & -4\frac{dk_1}{k_1}J_1(r_1k_1) & -4\frac{dk_2}{k_2}J_1(r_1k_2) & ... & -4\frac{dk_{N_f}}{k_{N_f}}J_1(r_1k_{N_f}) \\ 2r_2 & -4\frac{dk_1}{k_1}J_1(r_2k_1) & -4\frac{dk_2}{k_2}J_1(r_2k_2) & ... & -4\frac{dk_{N_f}}{k_{N_f}}J_1(r_2k_{N_f}) \\ ...... & & & & \\ 2r_{N_r} & -4\frac{dk_1}{k_1}J_1(r_{N_r}k_1) & -4\frac{dk_2}{k_2}J_1(r_{N_r}k_2) & ... & -4\frac{dk_{N_f}}{k_{N_f}}J_1(r_{N_r}k_{N_f}) \end{bmatrix} \begin{bmatrix} \epsilon_u \\ \epsilon_1 \\ \epsilon_2 \\ ... \\ \epsilon_{Nf} \end{bmatrix}.
$$
(26)

The large matrix on the RHS with the unknown parameters has size $N_r \times (N_f + 1)$. Thus the problem becomes one of solving a linear system of equations,

$$
\mathbf{Ax} = \mathbf{b},
$$
(27)

where $\mathbf{x}$ is the vector of unknown ϵs, $\mathbf{b}$ is the vector of observed SF3, and the $\mathbf{A}$ is the matrix formed by the particular relationship (equation 26) between them. Solving such system of equations is the subject of discrete inverse theory. Since we get to set N_r and N_f we can setup this problem as an under-determined ($N_r < N_f + 1$), even determined ($N_r = N_f + 1$), or over-determined (($N_r > N_f + 1$) problem. Here we decided to take the over-determined route, and find the solution using a form of the least-squares method.

F.2   Least-squares method

The least-squares method solves equation 27 by minimizing,

$$
||\mathbf{Ax} - \mathbf{b}||_2^2,
$$
(28)

the L-2 norm (mean square error). If we solve this optimization problem in MATLAB drectly using the \ operator, we obtain solutions presented in Figure SI-8.
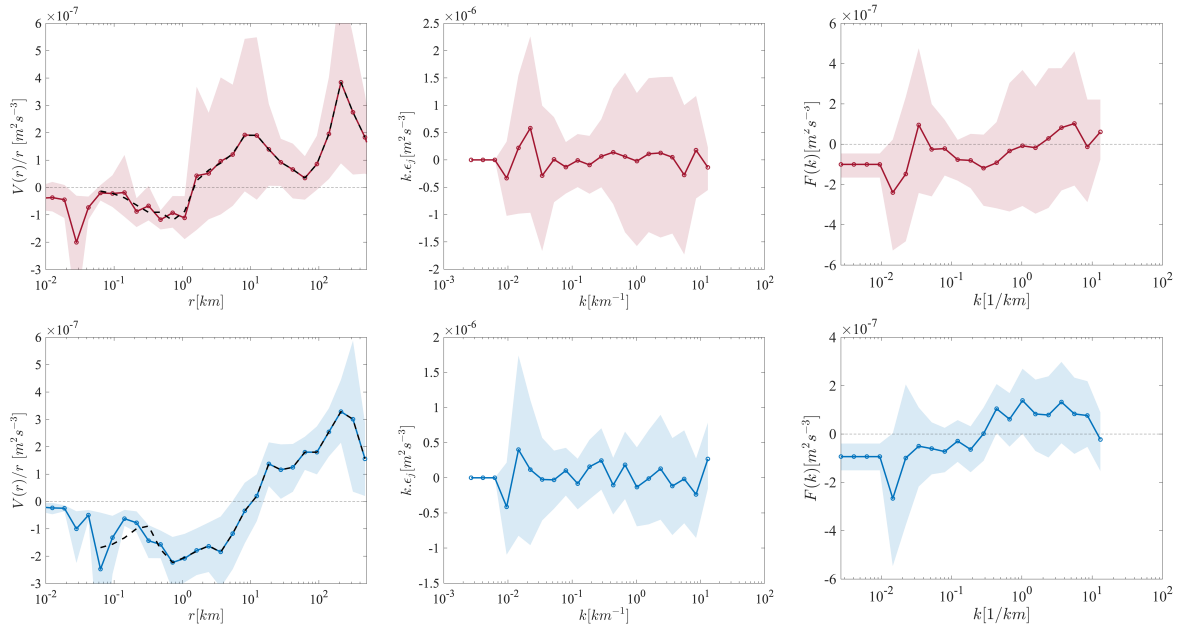
Figure SI-8: Fits to V(r) (dashed black line in first column) and parameter estimates using the least-square method for the GLAD (top) and the LASER (bottom) experiments.

The fitted $V(r)$ matches the observed $V(r)$ really well, capturing most of the details. The inferred energy injection is very variable and it is impossible to derive much physical insight from this. The estimated spectral flux is also quite variable, but a rough pattern of downscale flux at smaller scales and upscale flux at larger wavenumbers is suggested.

The problem with this solution is that the optimization method has over-fit the data, providing a really good fit to every detail but little insight. This problem is addressed by using regularization, where some penalty term is added to equation 28 to impose some additional physical constraints (like smoothness). The regularized solution can be designed to not all the stochastic variability in the observations, but instead only the broader pattern that might be more physically interpretable. One particular regularization approach that we used is discussed next.

F.3 Non-negative least-squares method (used here)

Here we use a particular type of regularization where it is assumed that all the parameters to be estimated are non-negative ($\mathbf{x} \geq 0$). Thus, we also assumed that ϵ_u and ϵ_j are all positive, and used the function *lsqnonneg* in MATLAB to solve the system (27). This assumption is equivalent to assuming that the spectral flux, F, is an increasing function. This is physically justified because we expect there to be an inverse cascade at smaller wavenumbers followed by a forward cascade at larger wavenumbers, and also expect the dissipation to take place at scales outside the observed range. The one downside of this assumption is there is some sink of kinetic energy over the fitted scales, like conversion of surface kinetic energy to potential energy, it will be artificially smoothed over. However as shown in the previous section, some regularization is necessary to derive more physical insight and so we chose this pragmatic approach. The solution from this method is shown in Figure 4 and discussed in the main text. In future work other regularization methods, like constraints only on smoothness, can be tried in the fitting procedure.

G Application to a simulation of rotating stratified turbulence

To show the efficacy of the above methodology at detecting the energy injection scales and the spectral flux, we first apply it to a numerical simulation of rotating stratified turbulence. The numerical simulation is of a 3D triply-periodic incompressible boussinesq equations, and were presented in (*50*). A mean constant stratification is prescribed. The external mechanical forcing is isotropic and generated randomly, applied in a shell of modes with wave numbers ($k_f = 10$).

This simulation was selected because it has the dynamical components that we expect to see in the ocean, we have precise knowledge of the energy injection, and a large range of scales
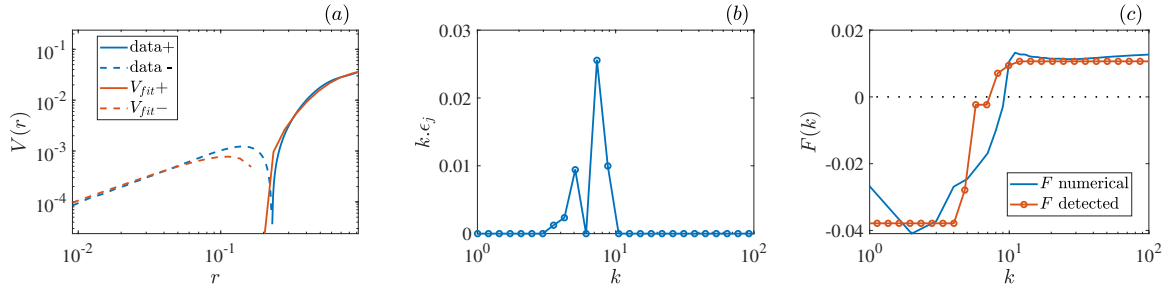
Figure SI-9: Fitting of the kinetic third-order structure function, the detected energy input and energy flux.

smaller than the forcing scale are resolved and simulate a downscale energy transfers. Also, more practically the qualitative structure of the V is similar to what is observed and shown in Figure 3; V is negative at smaller scales and positive at larger scales, and its absolute value approximately follows a linear power law (Figure SI-9a). We show that equation 25 can be fit quite well (red line in Figure SI-9a) to the model V, by optimizing the free parameters: the energy injection rates and scales (Figure SI-9b) and the upscale energy flux.

Furthermore, using the detected energy injection rate and the upscale energy flux we can reconstruct the kinetic energy flux in the spectral space, which is compared with that obtained directly from the numerical simulation in Figure SI-9c. Notice that the fitting only approximately matches the numerical $V(r)$ over the range of scales where it is negative, this is because $F(k)$ is not a perfectly monotonically increasing function. Implying that some small negative values of ϵ_j would be needed for a better fit, as should be expected given the slight decrease in F(k) at wavenumbers larger than 10. In fact, these scales are associated with a transfer from kinetic to potential energy. Our current method can not detect this detail. However, given the large uncertainty range associated with the observational $V(r)$, we should not expect to capture this level of detail even if we used an alternate method. The satisfactory fitting using our method implies that obtaining energy flux information from the third-order structure function is possible.